CHAPTER IV
RESULTS AND DISCUSSION

4.1 Characterization of Mesoporous Molecular Sieve

SEM images of calcined MCM-48 and MCM-41 are shown in Figure 4.1. The results were closely similar to the literature (Longloilert *et al.*, 2011; Reid *et al.*, 2001)

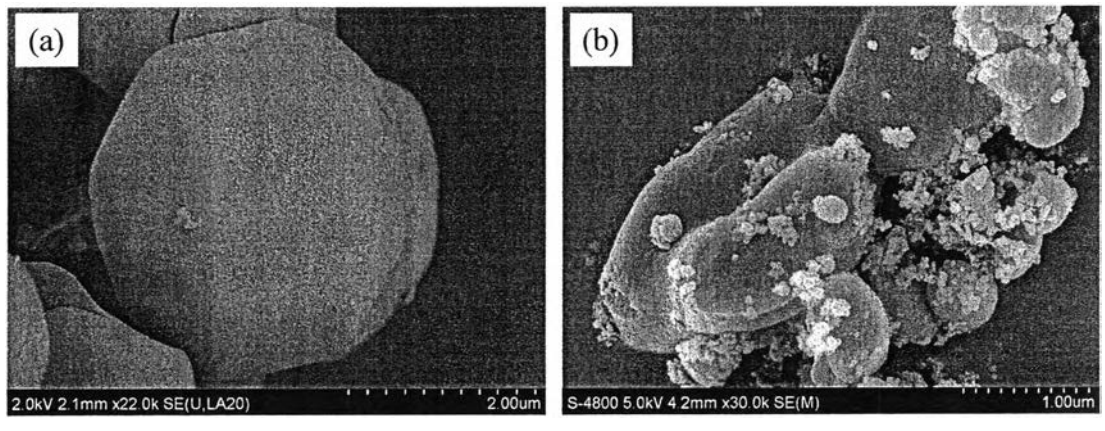

Figure 4.1 SEM images of the synthesized (a) MCM-48 and (b) MCM-41.

Figure 4.2 compares the typical XRD patterns of the synthesized MCM-48 and MCM-41. For MCM-48, the XRD pattern presents characteristic peak (211) and several other peaks, which can be indexed to the cubic (*Ia*3*d*) MCM-48 phase, as shown in previously studies (Longloilert *et al.*, 2011; Kim *et al.*, 2006; Nishiyama *et al.*, 2001). The XRD pattern of the synthesized MCM-41 consisted of the typical peaks at (100), (110) and (210), suggesting the hexagonal *p6* space group. This result was in agreement with the MCM-41 XRD pattern reported in elsewhere (Kim *et al.*, 2008; Thanabodeekij *et al.*, 2006).

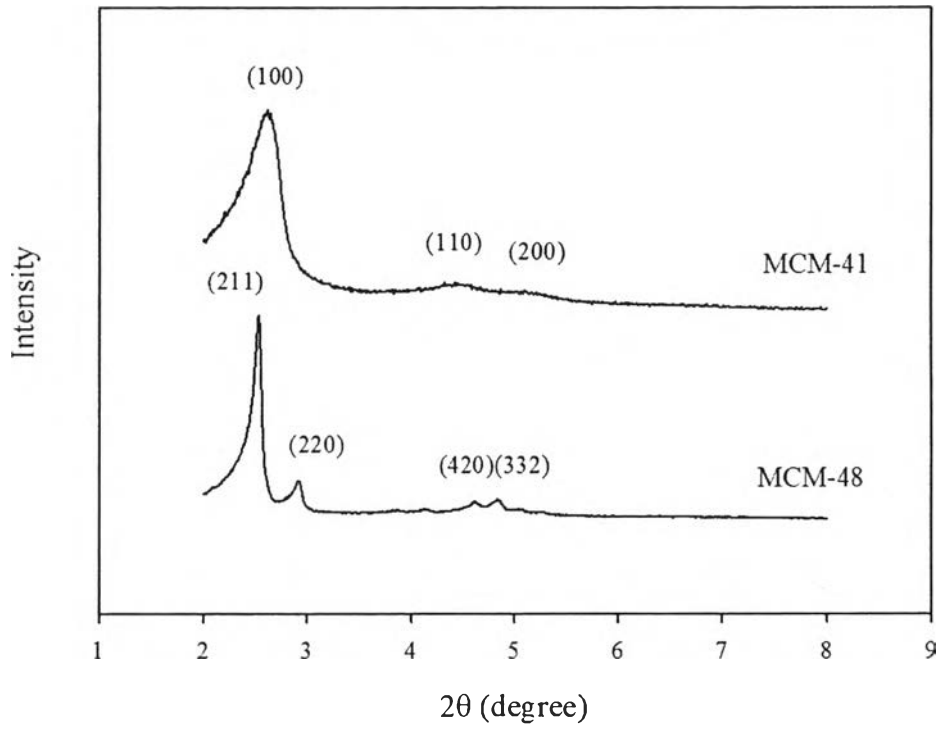

Figure 4.2 XRD spectra of the synthesized MCM-48 and MCM-41.

Physical properties in terms of specific surface area, pore volume, and pore diameter of the synthesized MCM-48 and MCM-41 are summarized in Table 4.1. The results indicate that MCM-41 and MCM-48 have high specific surface areas and high specific pore volumes. The pore structures of both mesoporous silica were highly uniform. MCM-41 exhibited a unidirectional pore system, composing of a regular hexagonal array of tubes while MCM-48 has a three dimensional pore system with the interlocking and bicontinuous pore system. (Longloilert *et al.*, 2011; Thanabodeekij *et al.*, 2006).

Table 4.1 Specific surface area, pore volume, and pore diameter of the synthesized MCM-48 and MCM-41

Sample	BET surface area (m^2/g)	Pore volume (ml/g)	Pore diameter (nm)
MCM-48	1288	0.92	2.86
MCM-41	1176	0.90	3.07

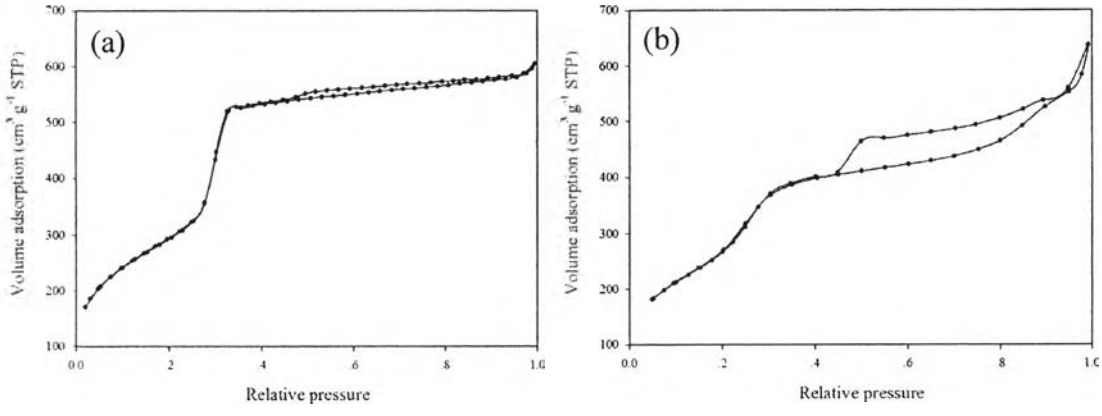

Figure 4.3 N_2-adsorption and desorption isotherms of (a) MCM-48 and (b) MCM-41.

The nitrogen adsorption–desorption isotherms of the calcined MCM-48 and MCM-41 are shown in Figure 4.3. Both silica exhibited type IV isotherms. The hysteresis loop in MCM-48 showed narrower range than that in MCM-41, indicating the more uniform pores in the cubic MCM-48. This result was in agreement with the literatures (Jang *et al.*, 2009; Kim and Marand, 2008).

4.2 Polybenzoxazine Membrane Properties

4.2.1 Structural Characteristics of Polybenzoxazine Membrane

The chemical structure of polybenzoxazine membrane was examined by ATR-IR and ^{1}H-NMR. The IR spectrum of PBZ membrane is shown in Figure 4.4. A symmetric stretchings of C–O–C (1228 cm^{-1}), C–N–C (1175 cm^{-1}), and CH_2 wagging of oxazine (1259 cm^{-1}) were observed. The characteristic absorption bands related to trisubstituted benzene ring were at 1495 and 929 cm^{-1}, attributing to out of plane bending vibrations of C–H. These IR results are in agreement with the study of Takeichi *et al.* (2005) and Pakkethati *et al.* (2010).

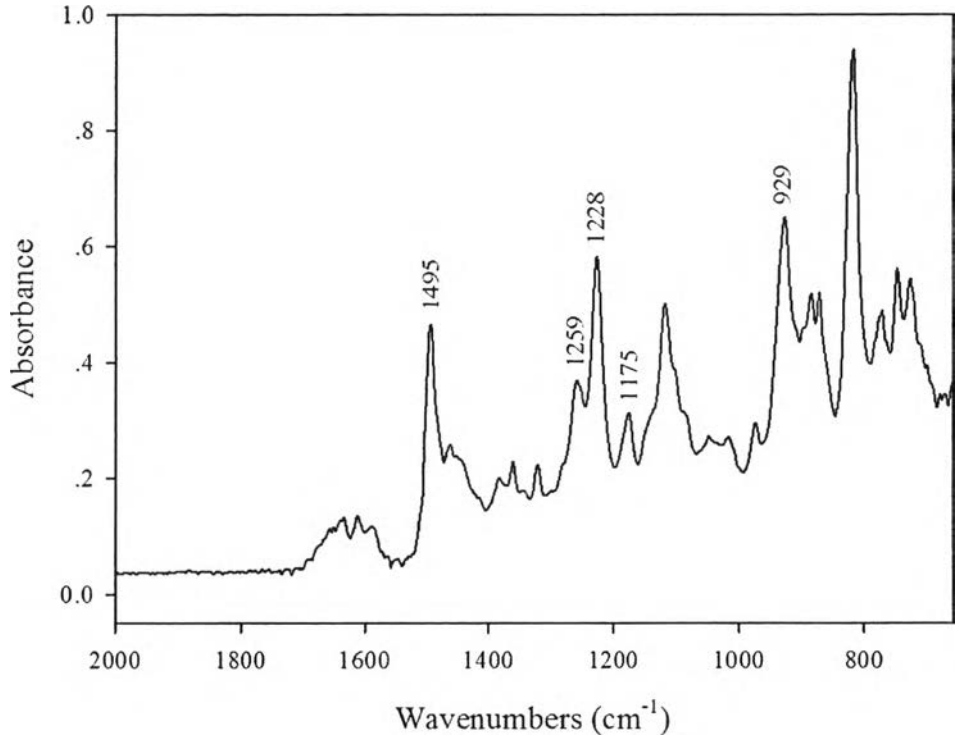

Figure 4.4 IR spectrum of the synthesized polybenzoxazine membrane.

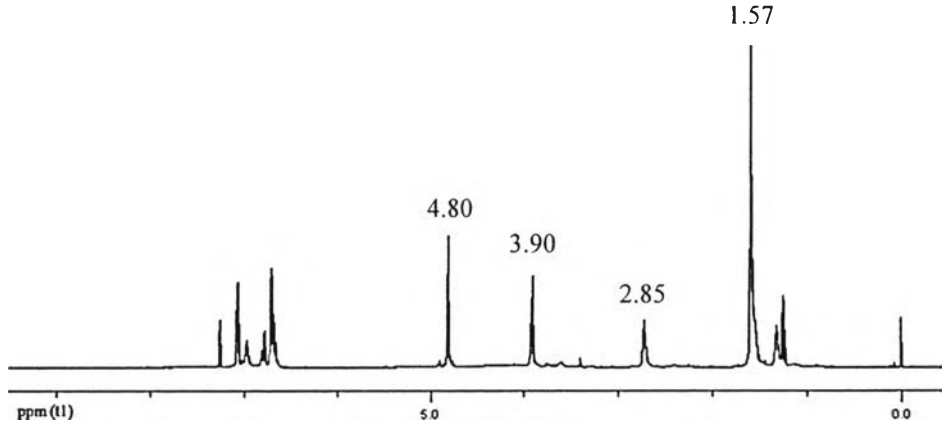

Figure 4.5 ^{1}H-NMR spectrum of the synthesized polybenzoxazine precursor.

The structure was also confirmed using ^{1}H-NMR measurement. The ^{1}H-NMR spectrum of the precursor is shown in Figure 4.5. The characteristic peaks assigned to methylene protons of O–CH_2–N and Ar–CH_2–N of oxazine ring were

observed at 4.80 and 3.90 ppm, respectively. The methyl protons of bisphenol-A were observed at 1.57 ppm. The methylene protons of the ring-opened benzoxazine were observed at 2.85 ppm. These results were consistent to those reported in the literature (Takeichi *et al.*, 2005).

4.2.2 Appearance and Morphology of Polybenzoxazine Membrane

The prepared PBZ film, showing its appearance and morphology in Figures 4.6 and 4.7 illustrates smooth surface and dense film.

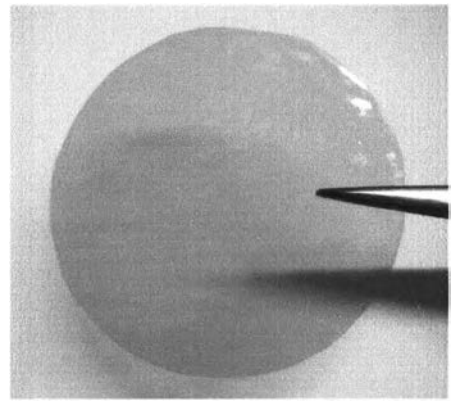

Figure 4.6 Appearance of the synthesized polybenzoxazine membrane.

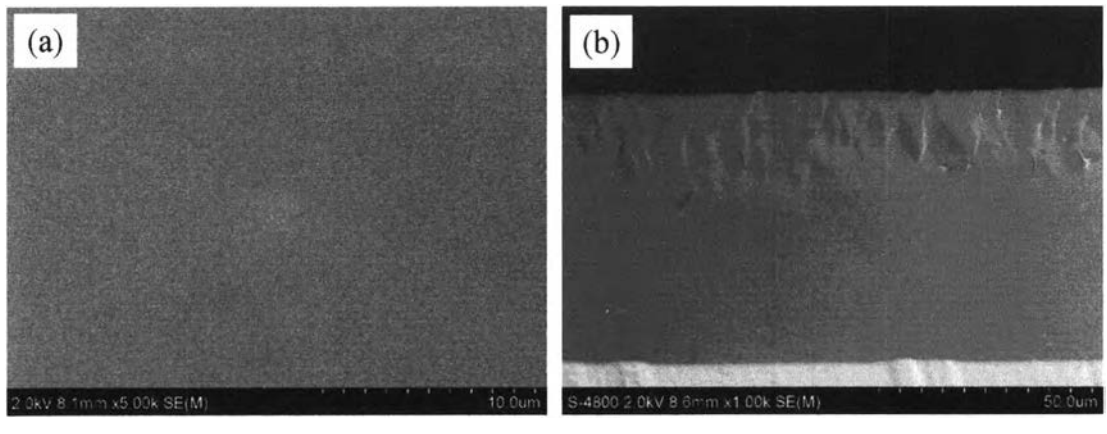

Figure 4.7 SEM micrographs of the synthesized polybenzoxazine membrane from (a) top view and (b) cross-section.

4.2.3 Thermal Behaviors of the Synthesized Polybenxozazine

The curing behavior of polybenzoxazine was investigated using DSC, and the result is shown in Figure 4.8. The DSC thermogram of partially-cured PBZ showed an exothermic peak which began at 160°C with a maximum at 220°C due to the ring-opening polymerization of benzoxazine precursor, as described in previous results (Takeichi *et al.*, 2005; Pakkethati *et al.*, 2010).

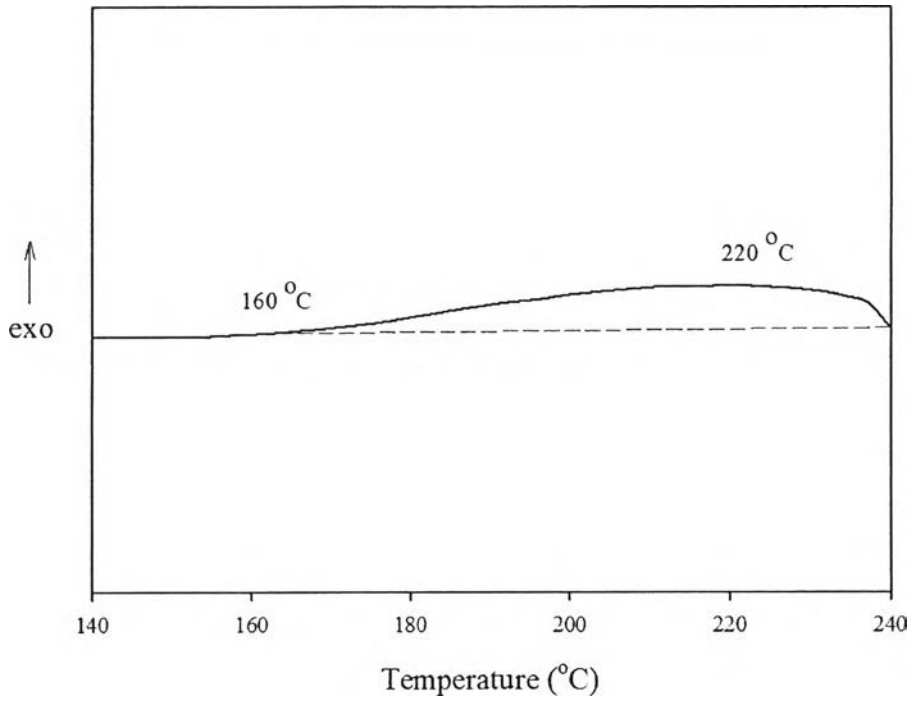

Figure 4.8 DSC thermogram of the synthesized polybenzoxazine precursor.

The TGA thermogram in Figure 4.9 showed the thermal stability of polybenzoxazine. The decomposition temperature started at around 275°C and the char yield was around 22%. The result is similar to those reported by Takeichi *et al.* (2005) and Pakkethati *et al.* (2010).

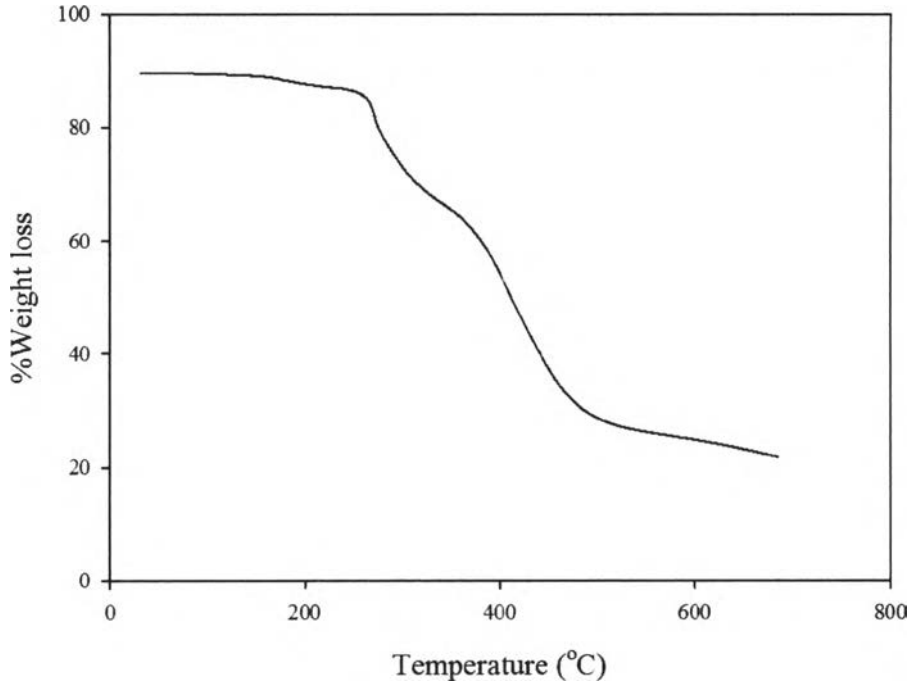

Figure 4.9 TGA thermogram of the synthesized polybenzoxazine membrane.

4.3 Mixed Matrix Membranes Properties

4.3.1 Appearance of Mixed Matrix Membranes

To improve the performance of the polymer membranes, the filled PBZ membranes with different MCM-48 loadings were studied. The appearance of the prepared MMM is shown in Figure 4.10.

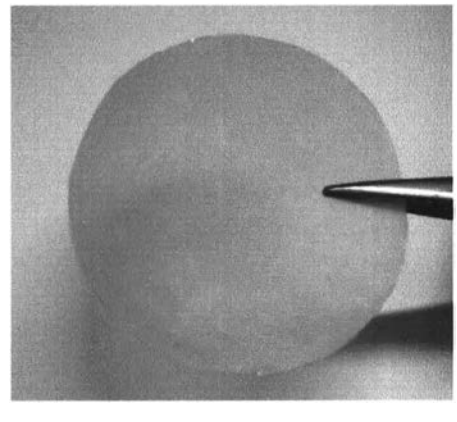

Figure 4.10 Appearance of mixed matrix membrane.

4.3.2 Interfacial Interaction of Polybenzoxazine and MCM-48

Figure 4.11 presents IR spectra of MCM-48, PBZ, and MMM. The IR spectrum of MCM-48 was closely matched with that of MCM-48 reported previously (Jang *et al.*, 2009; Kim *et al.*, 2005). The peak at 463 cm^{-1} represented Si-O bending vibration of the SiO_4 internal tetrahedral. The peaks at 796 and 962 cm^{-1} attributed to the Si-O-Si bending and the internal Si-OH, respectively. The peak at 1082 cm^{-1} represented Si-O-Si stretching, corresponding to the SiO_2 characteristic bands due to the vibrations of Si-O-Si bridges crosslinking in the silicate network, and was shifted to a lower frequency (1046 cm^{-1}) in MMM, attributing to Si-O-C linkage, meaning that the chemical bonding between MCM-48 and PBZ was formed.

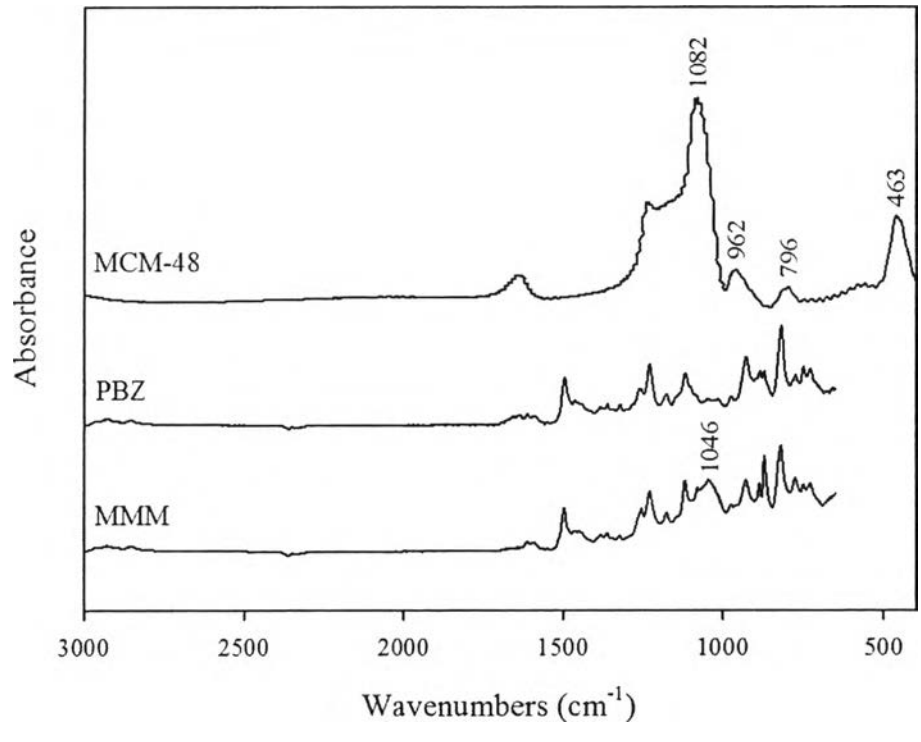

Figure 4.11 IR spectra of MCM-48, the synthesized polybenzoxazine membrane, and mixed matrix membrane.

SEM images of surface of MMMs in all cases, see Figure 4.12, show an increase in the roughness as higher MCM-48 was added to the polymer matrix.

However, the pictures clearly seem that MCM-48 was homogeneously distributed without large agglomeration of the particles in the membrane.

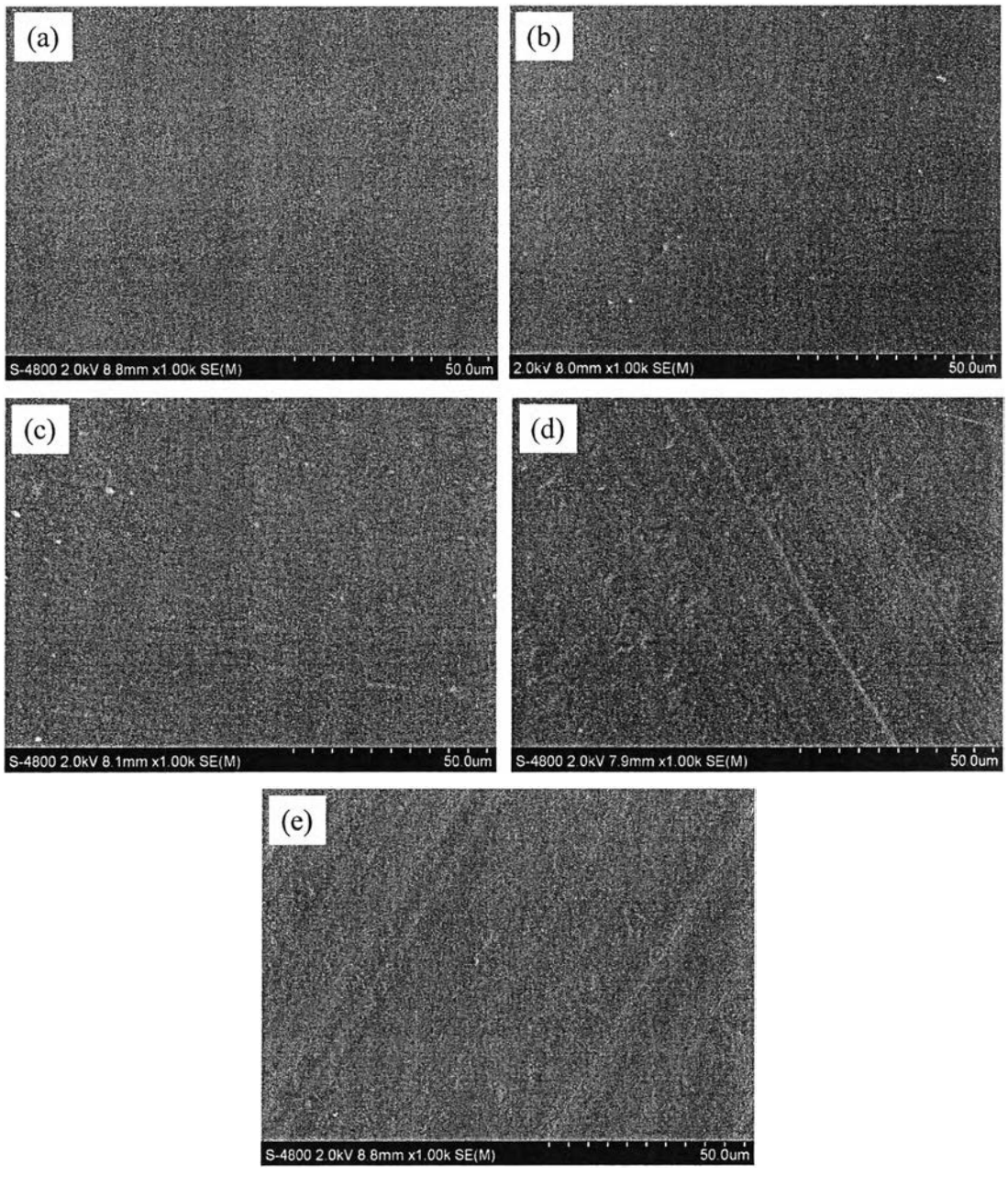

Figure 4.12 SEM micrographs of the PBZ membrane surface, containing various amounts of mesoporous MCM-48, (a) 1, (b) 5, (c) 10, (d) 15, and (e) 20 wt%.

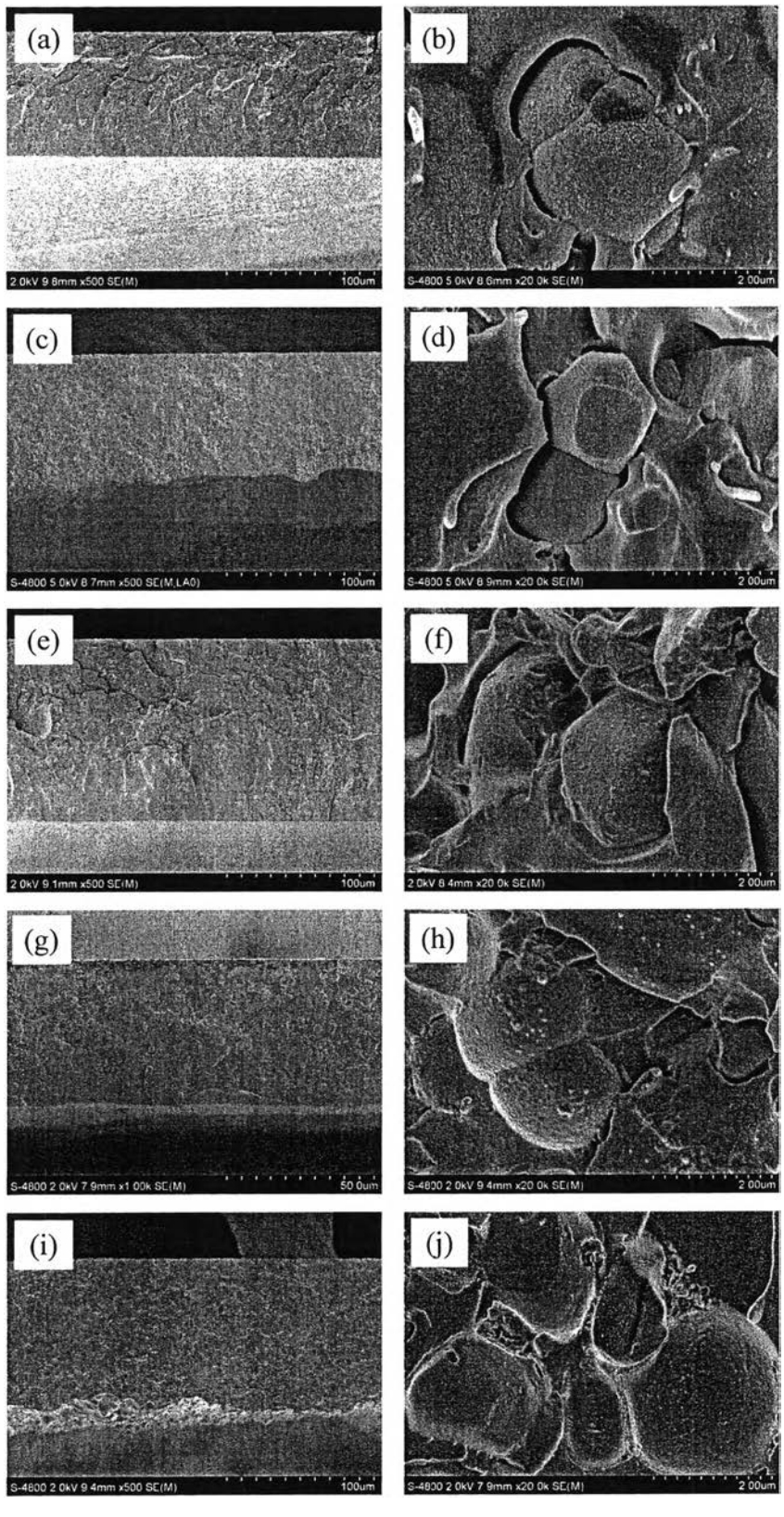

Figure 4.13 Cross-section SEM micrographs of PBZ membranes containing various amounts of mesoporous MCM-48; a, b) 1, c, d) 5, e, f) 10, g, h) 15, and i, j) 20 wt%.

The cross-section SEM images of polybenzoxazine membranes containing different loadings of the mesoporous MCM-48 are shown in Figure 4.13. The MCM-48 particles were homogeneously distributed inside the polymer matrix, as well. At higher magnification, Figures 4.13 (b) and (d) show the PBZ membrane with the MCM-48 loading of 1 and 5 wt%, respectively. There were voids around MCM-48 particles due to poor interaction between polymer and MCM-48 that could also be explained by the FTIR results in Figure 4.14. It shows IR spectra of the PBZ membranes containing different loadings of the mesoporous MCM-48. The Si-O-C peak at 1046 cm^{-1} increased as increasing the MCM-48 loading. At 1 and 5 wt% loadings (Figures 4.14 (a) and (b), respectively), the Si-O-C peak at 1046 cm^{-1} appeared with low absorbance, they provided poor chemical bonding between MCM-48 and PBZ. When increasing to 10 wt% loading, the Si-O-C peak increased dramatically because of a better interaction between the polymer and MCM-48 particles. This result is consistent with that reported by Zornoza *et al.* (2009) who prepared the mixed matrix membranes comprising polysulfone Udel®(PSF) matrix and ordered mesoporous silica spheres (MSS) as filler with loadings varying between 0 and 32 wt%. They found that the interaction between the polymer and the silica occurred with 8 wt% of MSS-PSF MMM. The FTIR spectrum of MMM showed one peak related to silica vibrations and another peak showing hydrogen bonding between the hydroxyl-rich surface and the aryl ether groups of the polymer.

At 10 wt% MCM-48 loading, see Figure 4.13 (f), there was no particles agglomeration, resulting in no void morphology. This is owing to good interface between the polymer and MCM-48 particles, as confirmed by the increase in Si-O-C peak in Figure 4.14 (c).Although, IR spectra of Figures 4.14 (d) and (e) show higher Si-O-C peak when increasing the loadings to 15 and 20 wt%, there were more voids observed at the interface between the polymer and MCM-48 particles, as can be seen in Figures 4.13 (h) and (j), respectively. This might be because of the polarity of both—PBZ was hydrophobic, while MCM-48 was hydrophilic—making the mixture become immiscible, as a result, it provided poor interaction.

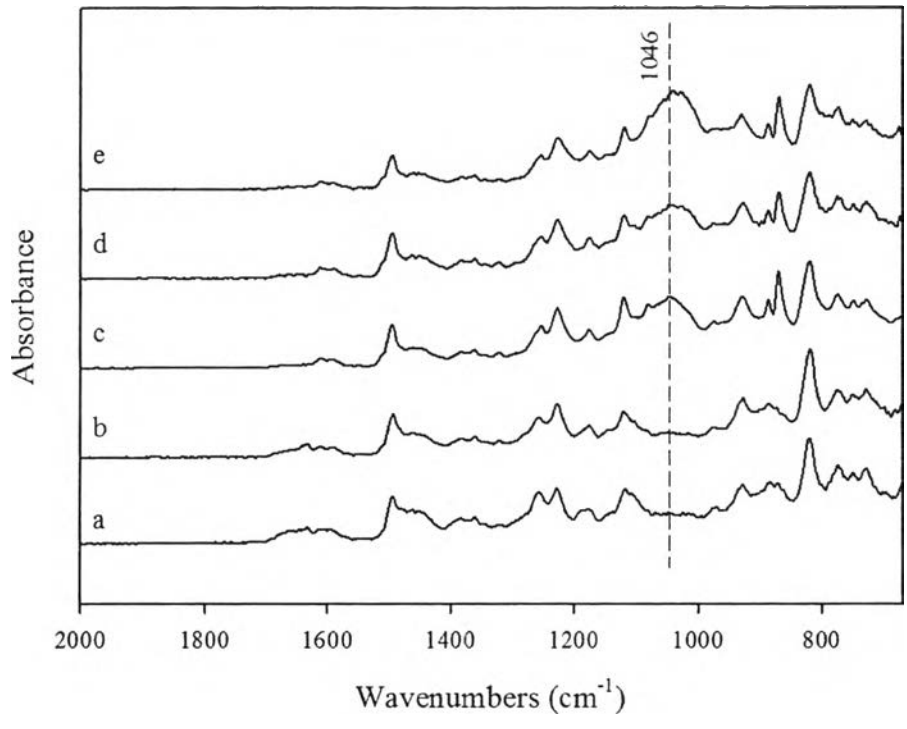

Figure 4.14 IR spectra of polybenzoxazine membranes containing various amounts of mesoporous MCM-48; a) 1, b) 5, c) 10, d) 15, and e) 20 wt%.

Table 4.2 Glass transition temperature (Tg) of PBZ and MCM-48/PBZ membranes

Membrane	Tg (°C)
Pure PBZ	205
10 wt% MCM-48/PBZ	230

The glass transition temperatures (T_g) of pure polybenzoxazine and 10 wt% MCM-48 MMM are presented in Table 4.2. The result shows the higher Tg value of MMM than that obtained from the pure polybenzoxazine membrane because the addition of inorganic filler introduced the higher silica network through hydrogen bonding interaction, which restricted the movement of polymer chains. Similar result was reported by Devaraju *et al.* (2011) who showed a higher Tg value of PBZ-silica hybrid nanocomposite than that of unmodified polybenzoxazine matrix.

4.4 Gas Separation Measurements

4.4.1 Effect of Filler Loading on the Gas Permeability

Polybenzoxazine membrane and MMMs were tested in the single gas measurements of CH_4 and CO_2. Table 4.3 summarizes the pure gas permeability results for the PBZ membrane and the MMMs. For the PBZ membrane, there were no CH_4 and CO_2 gases passed through the polymer matrix. As discussed earlier in the SEM images of pure PBZ, the film was very dense, thus no or very small voids in the membrane. The addition of MCM-48 particles into PBZ matrix, thus, resulted in improvement of the membrane performance. At 1 and 5 wt% loadings, both gases still could not penetrate through the membrane. It could be suggested that the amount of MCM-48 is not optimum, as explained previously. Moreover, in the previous works (Kim *et al.*, 2006; Kim and Marand, 2008) mesoporous molecular sieve of the M41S family with loadings in the 10–40 wt% range were needed.

Table 4.3 CH_4/CO_2 selectivity, gas permeance of CH_4 and CO_2 (GPU) using PBZ, MCM-48/PBZ, and MCM-41/PBZ membranes

Membrane	Permeance (GPU)		CH_4/CO_2 selectivity
	CH_4	CO_2	
Pure PBZ	0	0	0
1 wt% MCM-48/PBZ	0	0	0
5 wt% MCM-48/PBZ	0	0	0
10 wt% MCM-48/PBZ	452.50 ± 94.03	255.27 ± 54.60	1.78 ± 0.18
15 wt% MCM-48/PBZ	1304.95 ± 30.5	770.12 ± 52.65	1.70 ± 0.13
20 wt% MCM-48/PBZ	2144.55 ± 37.87	1331.80 ± 108.52	1.62 ± 0.17
10 wt% MCM-41/PBZ	22.04 ± 3.13	182.58 ± 20.73	0.12 ± 0.01

The permeance of CH_4 and CO_2 and the CH_4/CO_2 selectivity increased when loading 10 wt% of MCM-48 into the membrane. Comparing to the pure PBZ membrane, the CH_4 and CO_2 permeance of MMM increased due to the pore structure of MCM-48 particles, allowing gas molecules to pass through the membrane. Kim *et*

al. (2006) explained the factors affecting the increase of the permeability with the filler loading. It consisted of two factors: difference of permeability between filler and polymer and changes induced by the filler in polymer structure. The first factor came from the fact that gas transport could pass through the mesopore of the filler which is a typical Knudsen flow.

$$\Pi = \frac{1}{RT}\frac{g}{\delta}D^{Kn} \quad \text{with } D^{Kn} \sim T^{0.5}, \sim M^{0.5}$$

where Π is the permeance, R is the gas constant, T is the temperature, g is the geometrical factor, δ is the membrane thickness, D^{Kn} is the Knudsen diffusivity, and M is the molecular weight.

According to Knudsen diffusion, the permeance is inversely proportional to the square root of molecular weight (Nishiyama *et al.*, 2001; Zornoza *et al.*, 2011). In this study, by following Knudsen diffusion mechanism, the permeance of CH_4 was more than that of CO_2 because CH_4, having lower molecular weight than CO_2, thus transports faster. The result is similar to that reported by Nishiyama *et al.* (2001) (e.g. the permeance of CH_4 and CO_2 for MCM-48 membrane were about 1.2×10^{-7} and 0.9×10^{-7} mol $m^{-2}s^{-1}Pa^{-1}$,respectively.)

Additionally, the filler loading into the polymer matrix could be responsible for the selectivity improvement, as shown previously (Zornoza *et al.*, 2011). At 10 wt% loading, the CH_4/CO_2 selectivity increased, as compared with the pure PBZ membrane. This result suggests that the higher selectivity comes from the molecular sieving effect and the interfacial contact between the MCM-48 particles and polymer, as shown in Figures 4.13 (e) and (f), and confirmed by the FTIR results in Figure 4.14 (c).

The permeance and the selectivity factor results are shown graphically in Figures 4.15 and 4.16, respectively. The permeance of CH_4 and CO_2 increased with increasing MCM-48 loading, while the CH_4/CO_2selectivity decreased. The drop in CH_4/CO_2 selectivity could be explained by the cracking of interfacial surface of PBZ and MCM-48, as also indicated by the SEM analysis.

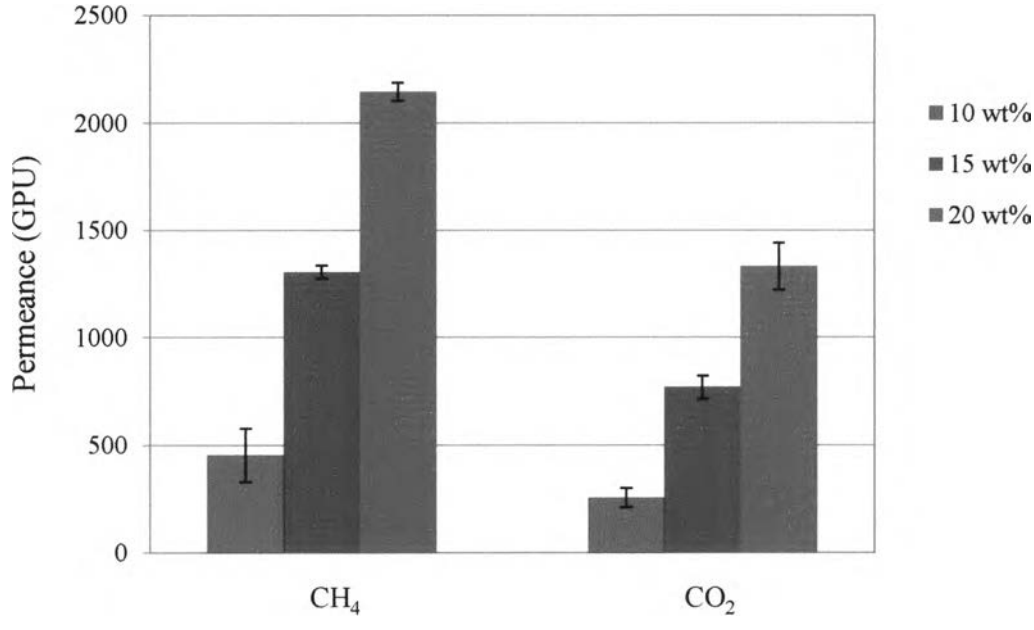

Figure 4.15 Pure gas permeances of MCM-48/PBZ membranes with different loadings.

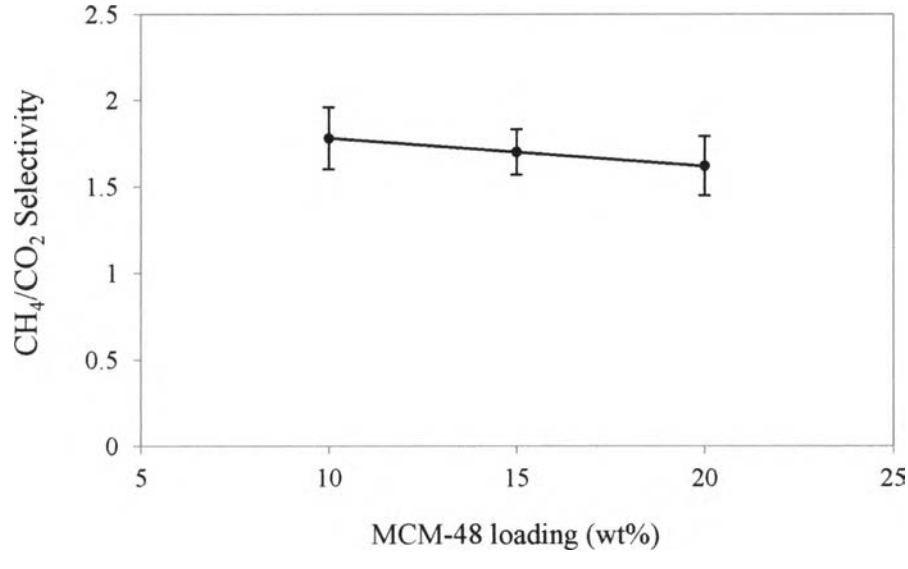

Figure 4.16 Selectivity of MCM-48/PBZ membranes at different loadings.

At the highest MCM-48 loading of 20 wt%, the CH_4 and CO_2 permeances of the membrane were more than those of the membranes with 10 and 15 wt% loading, suggesting that when the content of MCM-48 increased, the gas molecules diffused not only through the polymer matrix but also throughout the

interconnected particles of MCM-48, forming continuous pathways through the molecular sieve phase of MMM, as explained by Zimmerman *et al.* (1997). They suggested that higher membrane performance could be achieved if the MCM-48 particles formed small continuous pathways throughout the polymer matrix. Thus, the addition of 20 wt% MCM-48 provided higher chance for forming continuous pathways and allowed the gas molecules to diffuse throughout the filler component, resulting in higher gas permeance. For the polymer phase, the gas molecules were less permeable, as seen from the result of pure polybenzoxazine membrane. The results are in agreement with those reported by Kim *et al.* (2006). Moreover, the increase of the gas permeability resulted from the voids at the interface between the polymer and MCM-48 particles, as shown in Figures 4.13 (i) and (j).

In term of selectivity, 20 wt% loading provided lower the CH_4/CO_2 selectivity, as compared to 10 and 15 wt% loadings. This could be due to some interfacial cracking observed from the cross-section SEM images of the of MMM containing 20 wt% MCM-48 loading (Figures 4.13 (i) and (j)). The presence of the defect can be explained that the adhesion between the polymer and the filler is not strong enough, as also found by Kim *et al.* (2006) who added 20 wt% MCM-48 to PSF and found slightly decrease in the separation factor for all gases tested when comparing with 10 wt% loading. Zornaza *et al.* (2011) also obtained similar results when adding a higher content of mesoporous silica spheres (12-16 wt%), the selectivity was loss because of the generation of small non-selective voids existing between silica particles.

The differences in permeabilities of each MMM can be indicated by analyzing the contributions of diffusivity and solubility coefficients, using the following equations;

The diffusivity coefficient (D)

$$D = \frac{L^2}{6\theta}$$

The solubility coefficient (S)

$$S = \frac{P}{D}$$

where L is the thickness of membrane, θ is the intercept on the time-axis, and P is the permeability.

Table 4.4 Diffusivity (D) and solubility (S) of gases in MCM-48/PBZ membranes at different loadings

Membrane	CH_4		CO_2	
	D	S	D	S
10 wt% MCM-48/PBZ	3.25 ± 0.88	0.46 ± 0.07	1.58 ± 0.22	0.69 ± 0.11
15 wt% MCM-48/PBZ	3.93 ± 0.86	0.45 ± 0.12	2.76 ± 0.43	0.48 ± 0.03
20 wt% MCM-48/PBZ	5.84 ± 1.11	0.42 ± 0.11	3.98 ± 1.20	0.47 ± 0.13

D = 10^{-7}, cm^2/s. S = $10^{-7}cm^3$ at STP/(cm^3polymer atm).

The diffusivity and solubility for both CH_4 and CO_2 in MCM-48/PBZ membranes at different loadings are listed in Table 4.4. Both CH_4 and CO_2 diffusivity coefficients were shifted to higher values as increasing MCM-48 loading, causing the selectivity to shift to lower values. It can be concluded that, the gas permeability of the MCM-48-filled PBZ membrane was more strongly affected by the gas diffusivity than by the gas solubility. This result is in agreement with the study of Hu *et al.* (2006). Moreover, the increase in CH_4 and CO_2 diffusivities suggests that the diffusion of each gas is not affected by the molecular sieve channels, leading to higher permeability for both gases. This result is consistent to that reported by Kim *et al.* (2006). The increasing in permeability, after the incorporation of MCM-48 silica to the polymer, diffusivity, and solubility coefficients for all tested gases increased monotonically.

Additionally, the diffusivity and solubility coefficients could be explained the gas permeability of the membranes. The CH_4 diffusivity was more than the CO_2 diffusivity because CO_2 molecules are capable to interact with the polar surface of filler during the permeation, meaning that CO_2 is preferentially adsorbed and also transports slower than CH_4, and hence, the permeance of CH_4 was higher than that of CO_2.

4.4.2 Effect of Silica type (MCM-48 and MCM-41) on the Gas Permeability

According to the permeability results, the content of the filler on poly-benzoxazine membrane was an important factor in the performance of the membranes. In this study, the optimum amount of MCM-48 added to benzoxazine prepolymer to prepare MMM was 10 wt% loading. Zornoza *et al.* (2009) found that the MSS loading of 8 wt% was optimal in terms of H_2/CH_4 separation performance because the optimal formulation of inorganic filler-polymer was achieved by an increase in selectivities and permeabilities with the lowest filler percentage (e.g. the H_2/CH_4 selectivities of 8 and 32 wt% loadings were 79.2 and 33.6, respectively).

Interestingly, when comparing between MCM-41 and MCM-48, the amount of gas passed through the pores of MCM-48 was much higher than those passed through the pores of MCM-41. This is probably due to the three dimensional pore structure of the MCM-48, see Figure 4.17, allowing higher amount of gas to pass through. Moreover, from SEM images of MCM-41 membrane (Figure 4.18), MCM-41 particles were unevenly distributed in the membrane. There was large agglomeration of particles that caused a lower gas permeance. In addition, larger voids between the fillers and the matrix was observed, thus, the selectivity of this membrane was less than the case of MCM-48/PBZ membrane. The permeance and selectivity of MCM-41/PBZ membrane in Table 4.3 show that the permeance of CO_2 of MMM was more than that of CH_4. When comparing with the same composition of MCM-48/PBZ membrane, the CH_4 permeance was higher than the CO_2 permeance. This could be because of the shape of gas molecules (Figure 4.19) and the pore structure of molecular sieve. The configuration of CO_2 molecule is linear while that of CH_4 molecule is tetragonal, making the CO_2 molecule pass through the one-dimensional pore channel structure with a regular hexagonal array of tubes of MCM-41 easier. The CH_4 molecules, on the other hand, pass through the MCM-41 more difficult because of its configuration (Figure 4.19 (b)). Therefore, the CH_4 molecule could pass through the three dimensional pore structure of MCM-48 easier than the CO_2 molecules; as a result, the CH_4/CO_2 selectivity of MCM-41/PBZ membrane was less than that of MCM-48/PBZ membrane.

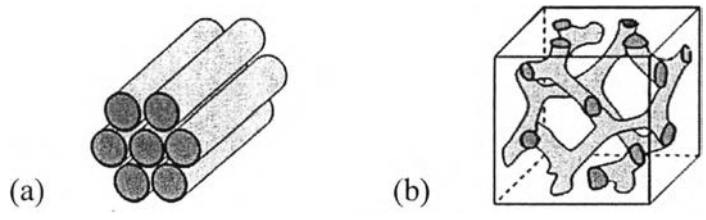

Figure 4.17 The structure of mesoporous materials (a) MCM-41 and (b) MCM-48 (Chew *et al*, 2010).

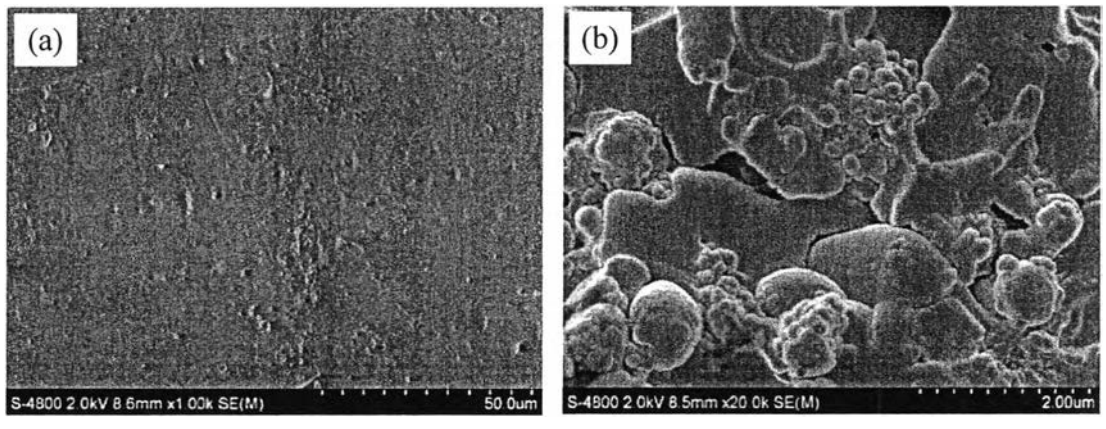

Figure 4.18 SEM micrographs of 10 wt% MCM-41/PBZ membrane from (a) top view and (b) cross-section.

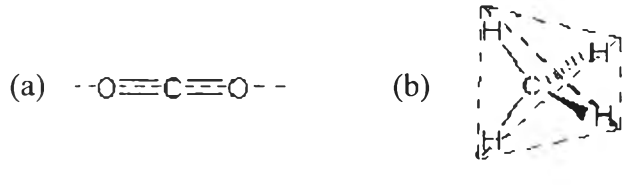

Figure 4.19 The shape of gas molecules (a) CO_2 and (b) CH_4 (http://www2.chemistry. msu.edu/faculty/reusch/VirtTxtJml/intro3.htm**).**